

DEVELOPMENT OF A PREDICTIVE DAMAGE METHODOLOGY FOR HYBRID WING BODY AIRCRAFT STRUCTURES

Hasan Raza, Christopher Harley, Pradeep Vaghela, and Javid Bayandor

CRashworthiness for **A**erospace **S**tructures and **H**ybrids (**CRASH**) Lab
Department of Mechanical and Aerospace Engineering
University at Buffalo - The State University of New York, NY, USA

Abstract

The aviation industry is constantly evolving and has taken a leading role in the integration of composite structures. This is particularly the case in the commercial aviation sector where fuel price constitutes a significant portion of the operational cost. In an effort to develop lighter, durable and more fuel-efficient aircraft, researchers at Boeing and NASA have collaborated to create the Pultruded Rod Stitched Efficient Unitized Structure (PRSEUS) that enables the development of damage tolerant Hybrid Wing Body (HWB) aircraft structures. Extensive testing has been carried out by NASA to demonstrate the performance and structural integrity of PRSEUS. To further understand the damage and failure mechanisms observed during the experiments, accurate analysis tools are required. This study focuses on the development of a comprehensive methodology to capture the behavior of stitched composite structures. The paper reports on the implementation of stitching in PRSEUS T-cap structures in order to predict its intra- and inter-laminar failure when subjected to critical loading conditions. Computational results are validated using benchmark experimental data.

Keywords: PRSEUS, Stitched Composites, Intra-laminar Failure, Delamination, Explicit Finite Element Method

1. Introduction

The aircraft industry is constantly working towards creating lighter, more fuel-efficient aircraft. This has led to increased investigations into composite materials as integral structural components of modern aircraft [1–3]. To further this advancement, the NASA Environmentally Responsible Aviation (ERA) project was created as part of which researchers at NASA Langley Research Center (LaRC) and The Boeing Company (Boeing) worked together to enable technologies that will reduce the impact of commercial aviation on the environment [4]. One of the major milestones for ERA was to assess the viability of the development of a Hybrid Wing Body (HWB) aircraft through the design, build and test of a Multi-Bay Box (MBB) test article, representative of an 80% scaled center section of one such innovative HWB concept [5]. Figure 1 shows NASA's N3-X design, projecting the future of HWB technology [6].



Figure 1 – N3-X aircraft concept [6].

DAMAGE METHODOLOGY FOR HYBRID WING BODY AIRCRAFT STRUCTURES

The novel Pultruded Rod Stitched Efficient Unitized Structure (PRSEUS) addressed the unique structural and manufacturing challenges associated with the HWB design and therefore selected as a viable option to develop the MBB from and to help further the HWB technology. The PRSEUS design consists of pultruded rods incorporated as reinforcements into structures made from unidirectional carbon fiber reinforced polymer (CFRP) composites through stitching [7]. The PRSEUS design consists of stringer, frame, and T-cap structures. The T-cap structure is an important design feature of PRSEUS, which provides connectivity of the corner joints between orthogonal panels, thereby enabling the development of complex structures such as the MBB assembly [8,9]. Figure 2 depicts the center keel of the MBB consisting of the PRSEUS components [5,10]. Highlighted on the right as a finite element (FE) model is the T-cap structure of this alternate center keel design. PRSEUS skin, frames, stringers, and tear straps are all stitched together, then infused and cured in an out-of-autoclave process.

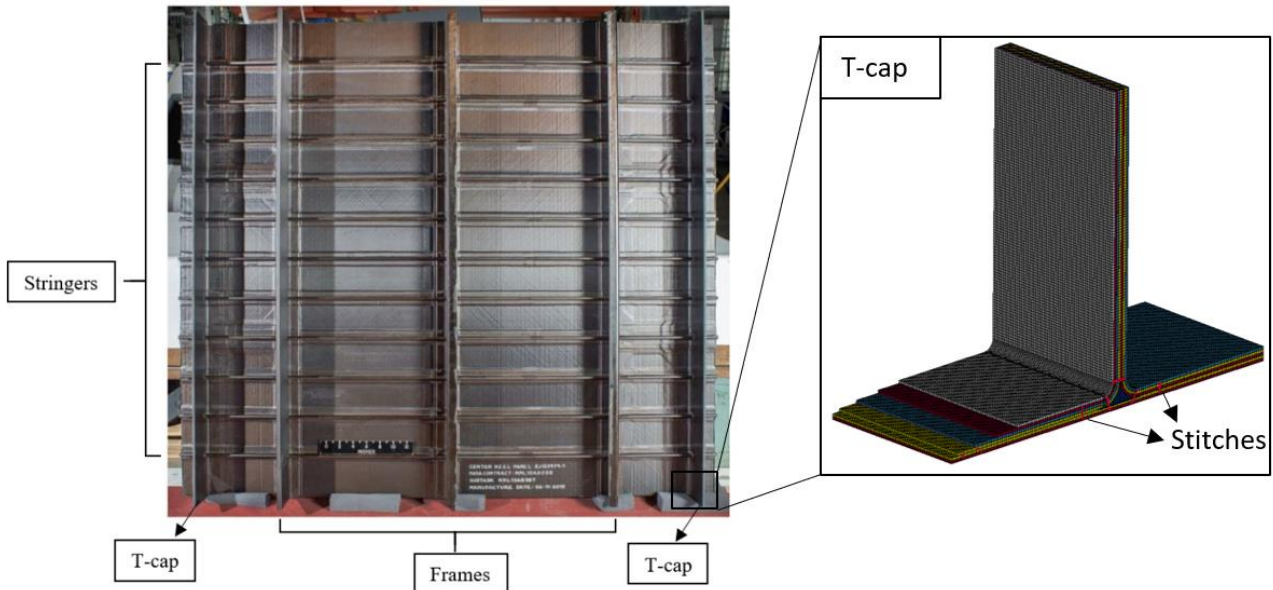


Figure 2 – Alternate center keel (adapted from [5]) with the T-cap model.

Although extensive experimental testing has been performed on PRSEUS to demonstrate its potential, there is still a need for efficient computational tools complemented by further validation testing before the technology can be further developed, commercially certified, and implemented [7]. The study presented here aims to contribute to further understanding and advancement of PRSEUS by developing a comprehensive damage methodology for its T-cap structure. Lovejoy and Leone [9] performed structural bending and tension tests on T-cap structures cut from the alternate center keel of the MBB. The current work focuses on the bending tests conducted on the baseline T-cap model with a single stitch row consisting of 1600 denier Vectran thread at the base of the web and no stringers. Abaqus and LS-DYNA (LS-Dyna), two commercially available FE software, were used to predict the bending behavior of the baseline T-cap structure. Implementation of stitches in CFRP composites was investigated with intra- and inter-laminar failure. Computational results were validated against available experimental data [9]. The predictive capabilities offered by these computational models can be used to contribute to future iterations of PRSEUS.

2. Experimental Testing

The T-cap structure is composed of the Class 72 Type 1 composite material. Each single stack (laminate) has a thickness of 0.052 in (1.3 mm) and consists of seven layers in [+45,-45,0,90,0,-45,+45] orientation with the percentages of 0, 45, and 90-degree fibers being 44.9, 42.9, and 12.2, respectively. Each layer is composed of AS4 fibers and VRM-34 epoxy. Stitches are formed from 1600 denier Vectran threads and the rod from Toray unidirectional T800/3900-2B fiber/resin system [5,7-8,10-12]. The baseline T-cap structure is shown in Fig. 3 [9]. The baseline T-cap with only one stitch row at the base of the T-cap web at the top of the fillet was the design used in MBB. The web

DAMAGE METHODOLOGY FOR HYBRID WING BODY AIRCRAFT STRUCTURES

is comprised of the stacks that wrap at its base to make the outer (exterior unpressurized side) and inner (interior pressurized side) flanges. A filler material, referred to as the noodle, is inserted into the empty cavity created by the flange wrap radii and skin stacks [9]. The T-cap specimen is displayed alongside with the FE model, highlighting the stitches and showing its laminate level details.

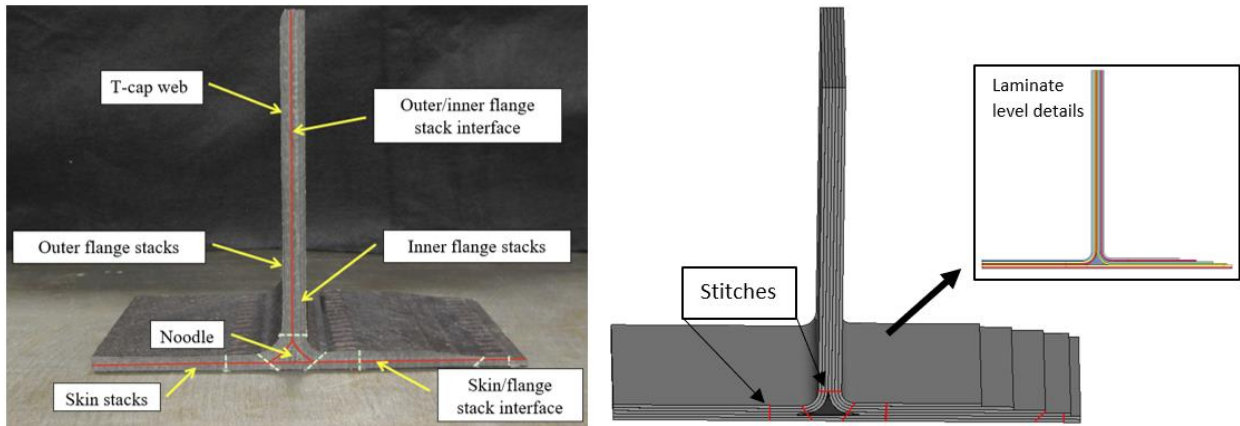


Figure 3 – Baseline T-cap specimen (adapted from [9]) and FE model on right.

The structure was tested for its failure loading in both bending and tension [9]. The specimens were nominally 2.9 in (73.7 mm) wide. The tests were performed in a 2.5-*kip* capacity load frame. The T-cap was bolted to an assembly attached to bolting slots at the base. Figure 4 depicts the bending test setup showing the pusher that applies the line load to induce bending. The tests were performed at ambient room temperature, and the load frames applied load under displacement control. Displacements were recorded using a linear variable displacement transducer (LVDT) and load versus displacement results were plotted [9]. The model is displayed with the boundaries simplified for efficient analysis. A fixed bound was used to model the clamped skin stacks while a constant displacement load was used to model the pusher arm. As indicated, the presented work will focus and refer to the results from bending tests.

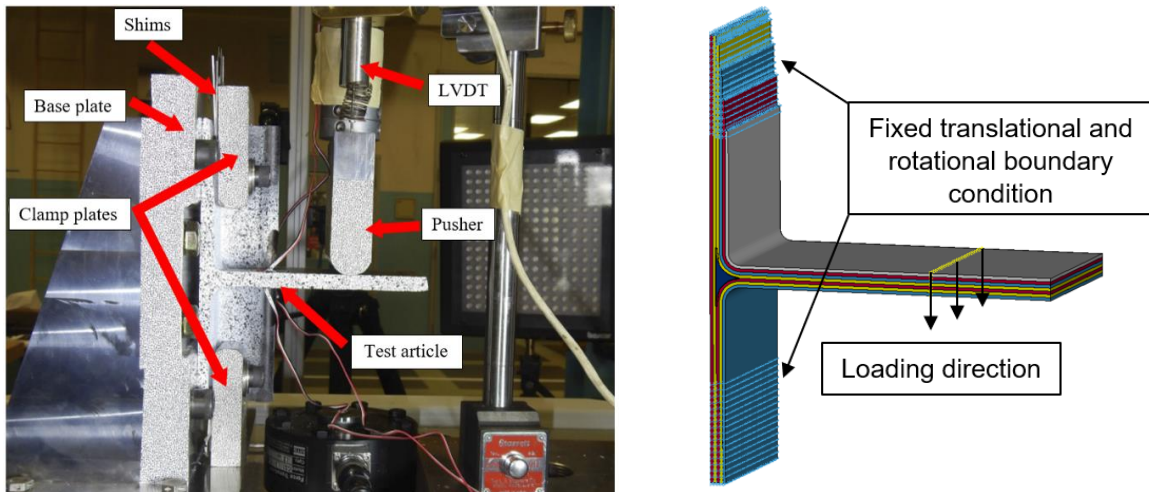


Figure 4 – T-cap bending test setup in the experiment [9] and FE model.

3. Computational Methodology

3.1 Composite Damage Modeling

Damage initiation, propagation, and failure modeling of composite materials can be complex when considering both intra- and inter-laminar failure. Such analyses have been made possible using advanced FE methods implemented in a number of commercially available software, such as Abaqus and LS-Dyna. Different modeling methodologies exist in terms of both composite damage models and failure criteria. Advanced composite material models are used to describe the linear

elastic response of the orthotropic, unidirectional CFRP composite laminates until failure occurs. After damage initiation, the laminates follow their respective comprehensive composite damage models as described in the following sections. Hereinafter, the finite element analysis (FEA) models investigated using Abaqus and LS-Dyna are referred to as Models A and B, respectively.

3.2 Model A - Abaqus Model

Hashin's [13–15] composite damage model is implemented in Abaqus and used to describe the CFRP laminate behavior. It identifies four modes of failure including fiber failure in tension and compression as well as matrix failure in tension and compression. Equations (1) to (4) describe the damage initiation criteria used in Abaqus for composite lamina [13]. When any of these criteria are met, the damage will begin to accumulate [16]. The primary driver of fiber damage is axial loading, while shear forces primarily drive the damage to the matrix.

Fiber tensile ($\hat{\sigma}_{11} \geq 0$) and compressive ($\hat{\sigma}_{11} < 0$) modes are defined as:

$$F_f^t = \left(\frac{\hat{\sigma}_{11}}{X^T}\right)^2 + \alpha \left(\frac{\hat{\tau}_{12}}{S^L}\right)^2 \quad (1)$$

$$F_f^c = \left(\frac{\hat{\sigma}_{11}}{X^C}\right)^2 \quad (2)$$

Matrix tensile ($\hat{\sigma}_{22} \geq 0$) and compressive ($\hat{\sigma}_{22} < 0$) modes are:

$$F_m^t = \left(\frac{\hat{\sigma}_{22}}{Y^T}\right)^2 + \left(\frac{\hat{\tau}_{12}}{S^L}\right)^2 \quad (3)$$

$$F_m^c = \left(\frac{\hat{\sigma}_{22}}{2S^T}\right)^2 + \left[\left(\frac{Y^C}{2S^T}\right)^2 - 1\right] \left(\frac{\hat{\sigma}_{22}}{Y^C}\right) + \left(\frac{\hat{\tau}_{12}}{S^L}\right)^2 \quad (4)$$

Where X^T is the longitudinal tensile strength, X^C is the longitudinal compressive strength, Y^T is the transverse tensile strength, Y^C is the transverse compressive strength, S^L is the longitudinal shear strength and S^T is the transverse shear strength.

Once the damage has initiated, the stiffness of the laminate begins to degrade based on the damage evolution properties defined. Prior to the initiation of damage, the response of the laminate is linearly elastic. The damage parameter takes the form of a multiplier to the stiffness matrix and softens the elastic response of the laminate over time. Equation (5) shows the damage stiffness matrix, described as C_d , where d_f is damage to the fibers, d_m is the damage to the matrix, and d_s is damage in shear. The damage stiffness matrix is updated at each step as damage accumulates in the laminate. Damage only extends and cannot return to an undamaged state.

$$C_d = \frac{1}{D} \begin{bmatrix} (1-d_f)E_1 & (1-d_m)(1-d_f)v_{21}E_1 & 0 \\ (1-d_m)(1-d_f)v_{12}E_2 & (1-d_m)E_2 & 0 \\ 0 & 0 & (1-d_s)GD \end{bmatrix}$$

where D is:

$$D = 1 - (1-d_m)(1-d_f)v_{12}v_{21} \quad (5)$$

Abaqus is known for its capabilities in implicit solving, but brittle materials like carbon composites and cohesive properties can prove challenging for the stability of the problem. Using viscous regularization, shown in Eq. (6), the material can be given some inherent resistance to large changes in states, yet dissipates some energy not accounted for in the damage evolution model [13]. This is achieved by forcing the tangent stiffness matrix to be positive at a small enough time increment enhancing stability even when the material is softening. The variable η is the viscosity term defining the relaxation time of the system and should be smaller than the stable time increment. The viscosity term stabilizes the implicit analysis, reducing the chances of divergence and increasing the stable

time increment. This allows cohesive and laminate models to soften before failure without requiring the use of the explicit method.

$$\dot{d} = \frac{1}{\eta}(d - d_v) \quad (6)$$

3.3 Model B - LS-Dyna Modeling

MAT54 enhanced composite damage material model is used in LS-Dyna to model the orthotropic unidirectional laminates. Its linear elastic stress-strain behavior is governed by Eq. (7) where the 1- direction denotes the fiber axial direction, 2- the matrix in the transverse direction, and 12- the shear direction [16,17]. Here, α is an input parameter that accounts for the nonlinear shear stress term, which must be calibrated whenever shear is present:

$$\varepsilon_1 = \frac{1}{E_1}(\sigma_1 - \nu_{12}\sigma_2) \quad \varepsilon_2 = \frac{1}{E_2}(\sigma_2 - \nu_{21}\sigma_1) \quad 2\varepsilon_{12} = \frac{1}{G_{12}}\tau_{12} + \alpha\tau_{12}^3 \quad (7)$$

Chang-Chang composite damage model [18] is used within MAT54 after the elastic region. It is an updated form of Hashin's composite damage model where it assumes that unidirectional CFRP behaves transversely isotropic in the fiber direction [15]. It contains a mode mixity term, β , also known as the shear stress weighing factor, which allows interaction between shear and normal failure modes. Chang-Chang damage model computes the stresses and damage progression of the fiber and matrix separately to determine the condition of an individual ply. It contains a set of non-physical input parameters which determine element failure and can be divided into three categories: erosion, crash-front softening factors, and parameters describing the material behavior after failure initiation [16–19]. The damage model is described by Eqs. (8) to (11) [20]:

Tensile fiber mode:

$$e_f^2 = \left(\frac{\sigma_{aa}}{X_t}\right)^2 + \beta \left(\frac{\sigma_{ab}}{S_c}\right)^2 - 1 \quad \begin{cases} e_f^2 \geq 0 \rightarrow \text{failed} \\ e_f^2 < 0 \rightarrow \text{elastic} \end{cases} \quad (8)$$

Compressive fiber mode:

$$e_c^2 = \left(\frac{\sigma_{aa}}{X_c}\right)^2 - 1 \quad \begin{cases} e_c^2 \geq 0 \rightarrow \text{failed} \\ e_c^2 < 0 \rightarrow \text{elastic} \end{cases} \quad (9)$$

where a is the fiber direction, b and c are the matrix and through-thickness directions. X_t and X_c are the fiber longitudinal tensile and compressive strengths, respectively, and e_f as well as e_c are the fiber failure parameter. σ_{aa} represents the longitudinal stress and σ_{ab} the shear stress of each layer. S_c denotes the matrix shear strength [7].

Tensile matrix mode:

$$e_m^2 = \left(\frac{\sigma_{bb}}{Y_t}\right)^2 + \left(\frac{\sigma_{ab}}{S_c}\right)^2 - 1 \quad \begin{cases} e_m^2 \geq 0 \rightarrow \text{failed} \\ e_m^2 < 0 \rightarrow \text{elastic} \end{cases} \quad (10)$$

Compressive matrix mode:

$$e_d^2 = \left(\frac{\sigma_{bb}}{2S_c}\right)^2 + \left[\left(\frac{Y_c}{2S_c}\right)^2 - 1\right] \frac{\sigma_{bb}}{Y_c} + \left(\frac{\sigma_{ab}}{S_c}\right)^2 - 1 \quad \begin{cases} e_d^2 \geq 0 \rightarrow \text{failed} \\ e_d^2 < 0 \rightarrow \text{elastic} \end{cases} \quad (11)$$

where Y_t and Y_c are the transverse tensile and compressive strength of the matrix. e_m and e_d are the matrix failure parameters that determine matrix cracking [17].

3.4 Cohesive Zone Model

Originated in the early 1960s, the cohesive zone model (CZM) [7,16,21] is based on the work by Dugdale [22] and Barenblatt [23,24]. It is one of the most widely used approaches to investigate interface bonding failure. CZM assumes a cohesive damage zone that develops near the crack tip

and uses strain energy release rate, G , during fracture formation to predict delamination [25]. It relies on the properties of the material, initial crack conditions, and a crack evolution function which describes the relationship between the normal and shear loads, to displacement. Once the interface reaches the maximum interface strength, σ^0 , which is the peak load on the stress-displacement relation, crack initiation begins in the model [25,26].

The modeling approach used in this study utilizes the bilinear stress-displacement relation as well as a mixed-mode relationship to represent the interactions between mode I, mode II, and mode III separations. The bilinear stress-displacement relation is shown in Fig. 5, where T and S are the normal and shear peak traction [25,27]. The area under the stress-displacement relation is equal to the energy release rate, G , or the fracture toughness, G_C , which is the critical value of G for delamination growth [28,29]. Energy release rates are assigned for both modes I and mode II. Mode III is assumed to be equal to mode II separation. Implementing the energy release rates for the modes of separation allows the cohesive model to utilize mixed mode capability which combines the energy release rates. The mixed mode capability is used in conjunction with a damage formulation (progressive softening) where mixed-mode displacement for total failure is computed using either Power law or Benzeggagh-Kenane (B-K) criteria [30]. Softening of the interface bonding occurs when the separation and sliding between layers exceeds the softening strain δ^0 . When the failure strain, δ^F , is reached the cohesive bond fails, and delamination initiates [16,25].

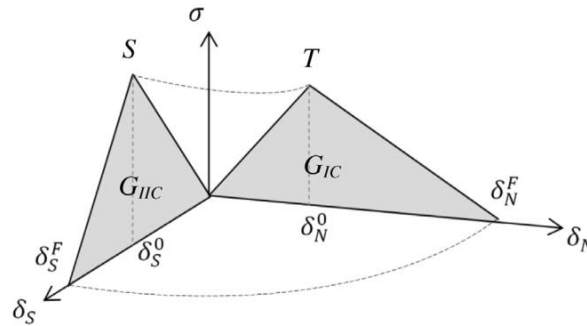


Figure 5 – Bilinear stress-displacement [25].

The distance from the tip of the crack to the point where the maximum stress is achieved is referred to as the cohesive zone length, l_{cz} . The cohesive zone needs to be discretized by enough elements, such that the distribution of load ahead of the crack can be represented correctly in FEM. Turon et al. [24] suggest using a minimum of 3 elements in the cohesive zone, however such fine mesh requirements can make structural analysis computationally expensive [25]. An alternative is to reduce the normal and shear peak loads which allows the use of an appropriate cohesive zone length without making the mesh overly fine [16,25–27].

3.5 Cohesive Interactions (Tiebreak contact)

An alternative to the CZM model is the cohesive contact algorithm implemented in both Abaqus, referred to as cohesive contact behavior, and LS-Dyna, referred to as Tiebreak contact. It uses a segment-based method to model theoretical interlaminar bonding based on the normal and shear peak stress. Tiebreak algorithm in LS-Dyna uses the Dycoss Discrete Crack method [31]. Both in Abaqus and LS-Dyna, the methods utilize a bilinear stress-displacement relation similar to the cohesive zone model. This is used in conjunction with a damage formulation where mixed-mode displacement for total failure can be computed using either Power law or B-K criteria [30]. Since no layer of cohesive elements is required to be modeled or defined at the interface, this approach becomes computationally less expensive when compared to the CZM model. Figure 6 shows the differences between the cohesive zone model and the cohesive contact algorithm.

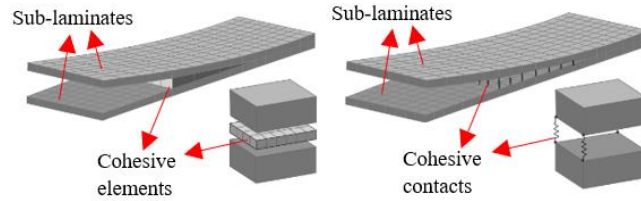


Figure 6 – Cohesive elements and contact comparison (*adapted from [32]*).

3.6 Stitching

PRSEUS is fabricated using a one-sided stitching technology instead of a conventional two-sided stitching approach. Figure 7 illustrates the stitching pattern utilized in PRSEUS [7]. Two needles are operated from the same side of the laminate, with one inserting the thread and the other catching the loop and pulling it back through the other side [7].

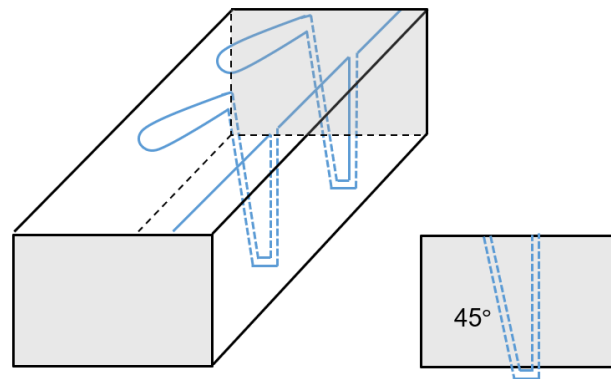


Figure 7– Illustration of the stitching patterns utilized in PRSEUS (*adapted from [7]*).

To effectively model and implement stitching in the T-cap structure, two fundamentally different methods were considered. The first method, referred to as the cohesive method, utilizes the cohesive interaction (tiebreak algorithm in LS-Dyna) approach to model both the stitches and the epoxy. Cohesive models are known to represent stitch bonding [7,33]. There are some underlying limitations to this approach which include its mesh-dependency and only being able to approximate some aspects of the unique stitching configuration. Similar limitations to this method are noted by Horton [7]. This method also does not account for the through-thickness stress concentration which is present during testing in the T-cap at the stitch locations.

The second approach, referred to as the 1-D element approach, utilizes individual 1-D element models to represent each individual through-thickness stitch. This approach does not model actual penetrations in the laminates, instead connects the nodes of both sides of the stitch location with a 1-D element such as a beam. This method allows the capture of the through-thickness tension effect and is less mesh-dependent compared to the above-mentioned cohesive method. Due to the absence of any direct connection to the interlaminar bonding, this method depends on the local stress concentration as well as friction to simulate the effect of a stitch [7]. For this study, the 1-D element approach was utilized to model the individual stitches due to its apparent advantages. Different 1-D elements were used in Abaqus and LS-Dyna with linear elastic properties to represent the stitching based on the material properties available from the manufacturer [7,34].

4. Model Validation

This section details the approach used to validate the interlaminar cohesive bonding for predicting delamination and stitch modeling methodology for the T-cap structure. Delamination modeling and stitch modeling methodologies are validated using available experimental data [35–38].

4.1 Delamination Validation

ASTM D-5528 [28] test is the standard test method for determining the opening Mode I interlaminar fracture toughness, G_{IC} , of unidirectional fiber-reinforced polymer matrix composites using double cantilever beam (DCB) specimen. It has been widely used to evaluate the interlaminar adhesive properties of laminate epoxies. The DCB specimen consists of a rectangular uniform thickness, unidirectional laminated composite containing a non-adhesive insert on the midplane which serves as a delamination initiator. Opening forces are applied using hinges or loading blocks bonded to the specimen. To establish an accurate delamination modeling methodology, both the cohesive zone model (CZM) and cohesive interaction (Tiebreak algorithm) were investigated. A standard DCB test was modeled and computational results were compared with the reported experimental data from Camanho and Dávila [35].

Multiple configurations of the DCB model were created to test the different element formulations, element types, and mesh sizes with respect to the interlaminar bonding approach. This trial and error approach provided a methodology that yielded good results with minimum compromise on accuracy and computational cost, which was an important consideration factor. The final iteration of the model in Abaqus consisted of linear, reduced-integration, quadrilateral shell element (S4R) with the Discrete Kirchhoff (DK) constraint [13]. The final iteration of the model in LS-Dyna consisted of the Belytschklo-Wong-Chiang shell elements governed by first-order shear deformation plate theory and incorporating warpage control [20,25]. Models included T300/977-2 carbon fiber reinforced polymer laminates that were 150 mm long, 20 mm wide, and 1.98 mm thick with an initial crack length of 55 mm.

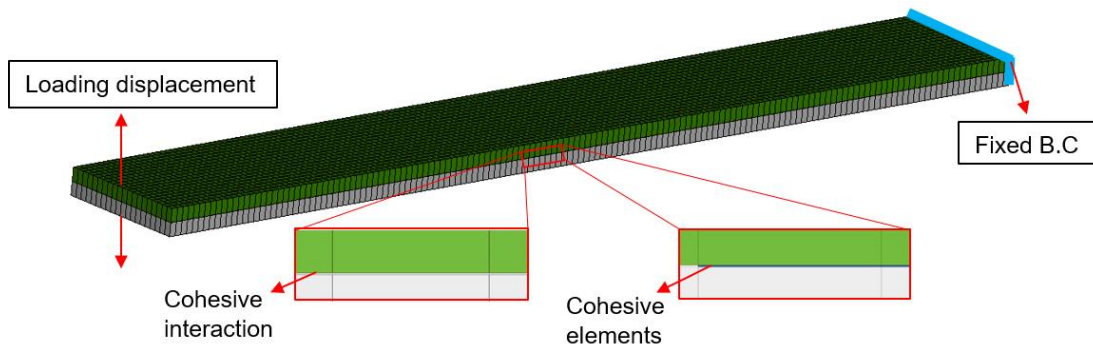


Figure 8 – FE model of DCB test setup showing CZM and cohesive interaction approach.

The cohesive elements for the cohesive zone model (CZM) were represented using an adhesive layer of three-dimensional (3-D) elements between the two laminates. Figure 8 shows the DCB test setup for both CZM (using 3D solid elements) and cohesive interaction contacts with artificial thicknesses applied to the sub-laminates. It should be noted that two different DCB models were setup for the two respective delamination modeling approaches, but are shown from a single DCB setup in Fig. 8 to avoid repetition. Loading was applied to the ends of the laminates in the opposite directions to replicate pulling at a constant displacement. Implicit analysis was used in Abaqus. To apply Dycoss Discrete Crack model however, LS-Dyna’s explicit solver needed to be utilized. The load applied and the total opening displacement were recorded to investigate the behavior of the laminates.

Figure 9 compares the DCB simulation results obtained using the implicit analysis in Abaqus with the experimental data, while Fig. 10 compares the same experimental data with the explicit analysis results from LS-Dyna. For clarification, the theoretical inter-laminar bonding approach is referred to as cohesive interactions for Model A and Tiebreak for Model B. Table 1 provides the percent errors calculated for the test results. The percent differences in the peak force, breaking displacement, and fracture energy release rate are found to be near 10 %, which can be accepted. The location of the peak force and breaking displacement generally matches the experimental data. The results further highlight an acceptable cumulative error in the total fracture energy. In both models, hourglass energies were found to be negligible (<10%).

DAMAGE METHODOLOGY FOR HYBRID WING BODY AIRCRAFT STRUCTURES

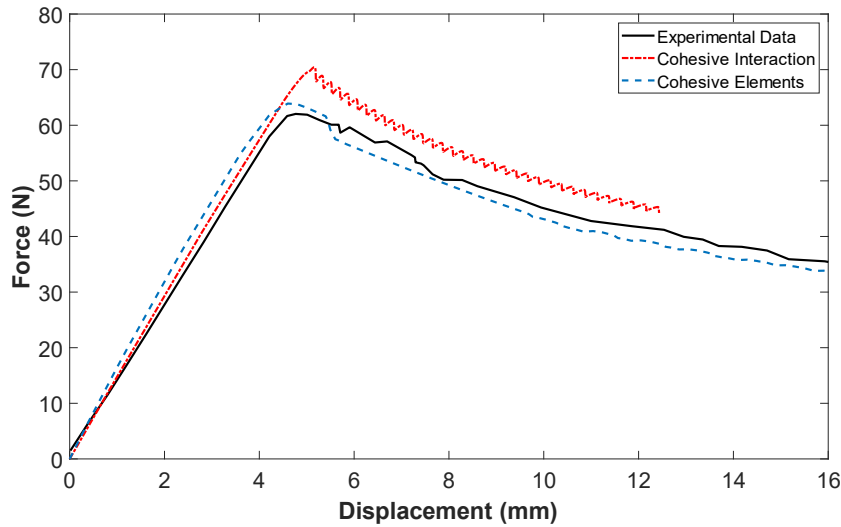


Figure 9 – DCB simulation results using Abaqus model with implicit analysis (test data from [35]).

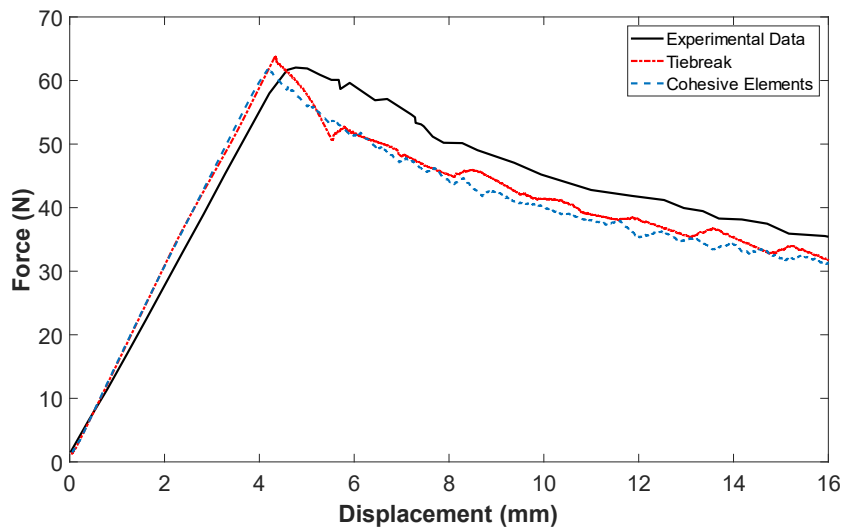


Figure 10 – DCB simulation results using LS-Dyna model with explicit analysis (test data from [35]).

Table 1 - Percent error comparison.

Model	Approach	Peak Force (%)	Breaking Displacement (%)	Fracture Energy Release Rate (%)
Model A (Abaqus)	Cohesive Elements	3.00	8.06	3.94
	Cohesive Interaction	13.50	3.50	3.23
Model B (LS-DYNA)	Cohesive Elements	10.06	9.00	10.06
	Tiebreak	8.71	12.57	8.71

It was observed that Model B produced slightly larger errors, likely due to the explicit nature of the simulation in comparison to Model A, which was implicit and therefore more suitable for a quasi-static simulation. To further investigate the delamination modeling methodology adopted, DCB simulations were run using fully integrated solid and cohesive elements (CZM approach) in both Abaqus and LS-Dyna using implicit analysis. Figure 11 shows the DCB simulation results with cohesive elements using implicit analysis for both Model A and Model B. The differences in peak force and breaking displacement were found to be less than 1%, matching the experimental data well. The results for the DCB tests show a very small cumulative error in the total fracture energy. The improved results came with a higher computational cost in comparison with using shell elements

and cohesive interaction (Tiebreak). Given the complexity of the full-scale T-cap structure and the number of plies involved, the less computationally expensive cohesive interaction (Tiebreak) was selected as the delamination modeling approach.

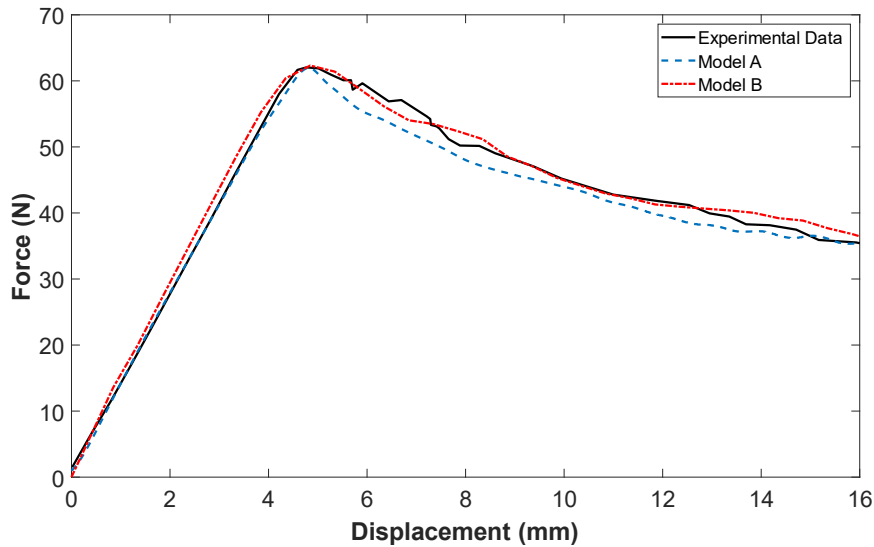


Figure 11 – DCB results with cohesive elements using implicit analysis (*test data from [35]*).

4.2 Stitch Model Validation

To develop and validate an effective stitch modeling methodology, a multi-step approach was used due to the lack of direct experimental data on the 1600 denier Vectran thread. The multi-step approach utilized the available experimental data from the literature to test and validate a way that a single stitch could be modeled in both Abaqus and LS-Dyna accurately. The first step involved using tensile test data from a single carbon fiber filament to verify the suitability of the FE platform applied. 1-D models were developed in the FE environment to assess whether small and thin single carbon fiber specimens could be represented. The breaking load and displacement were recorded and compared with the experimental data. A beam element was used to model the single carbon fiber filament in the LS-Dyna model, whereas a truss element was used in Abaqus. After validation, the second step aimed to apply the same methodology to verify a single filament of the Vectran thread by predicting its failure load and displacement accurately. The final step applied the established methodology to investigate whether the behavior of a multi-filament Kevlar yarn could be predicted. If the methodology could predict the behavior of a multi-filament Kevlar yarn, then it should theoretically be able to predict the response of a multi-filament Vectran thread to a reasonable extent.

4.2.1 Single Carbon Fiber Strand

A tensile test was replicated using FE similar to that performed by Kumar et al. [36] for a 60 mm long single carbon fiber. Figure 12 depicts the tensile test setup used in the analysis showing a scaled-up visualization of the 1-D element. Load and displacement histories were recorded and compared with the experimental data to validate the 1-D element model. Figure 13 compares Models A and B results with the experimental data. Overall, the results show good agreement with the test. Failure displacements of the FE models are within the same range as those of the experiments, with the failure force being within 2% range. Experimental results of the single carbon fiber show some hardening just before the failure. It is observed that their modulus increases over time such that near their breaking point, their tangent modulus is found to be higher than Young's modulus. This is something that the FE models are not able to capture due to their limited capabilities, however, the results are still in proximity.

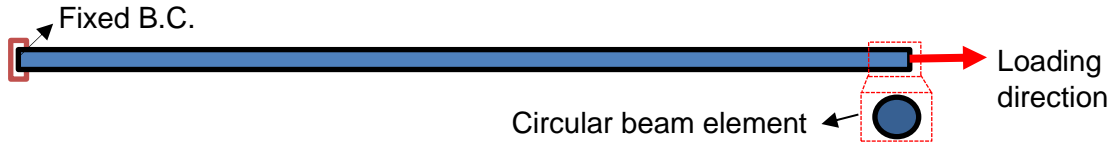


Figure 12 – Tensile test setup in FEA for 1-D element.

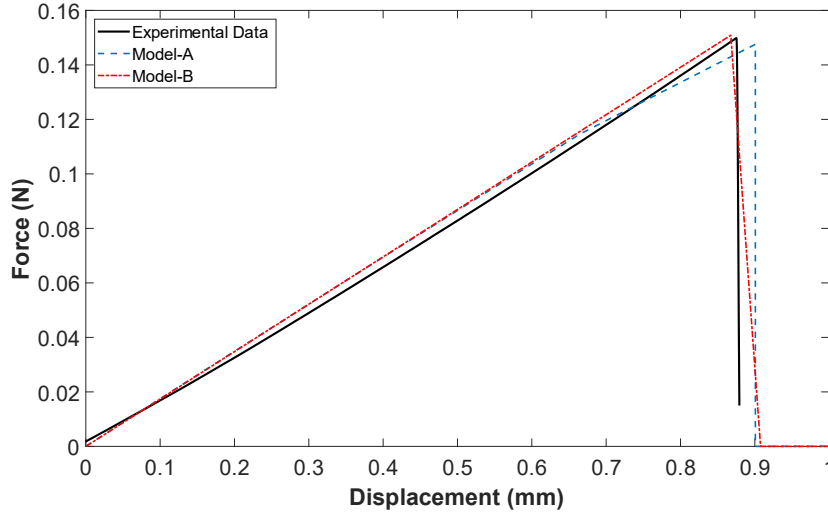


Figure 13 – Simulation results compared with single carbon fiber test (test data from [36].)

4.2.2 Single Vectran Filament

With an established approach for predicting failure in a single carbon fiber, the methodology was applied to a single Vectran filament. Tensile test data for a single Vectran fiber were taken from Pegoretti et al. [37] where a single filament of Vectran HS of 1500 denier was tested. The length of the test article was 25 mm with a diameter of $24.0 \pm 1.4 \mu m$. Figure 14 compares the results of Models A and B with experimental data. Similar behavior to that of the single carbon fiber result was observed, but more prominent where the tangent modulus of the Vectran filament found -using the experimental data near the breaking point, becomes higher than its recorded Young's modulus due to hardening. Nonetheless, the results match well in terms of breaking load and displacement, found to be within a margin of error of 1%. The fracture energy release rate had a higher error, which is expected since the FE models do not account for the hardening effect of Vectran filaments in the load and displacement history.

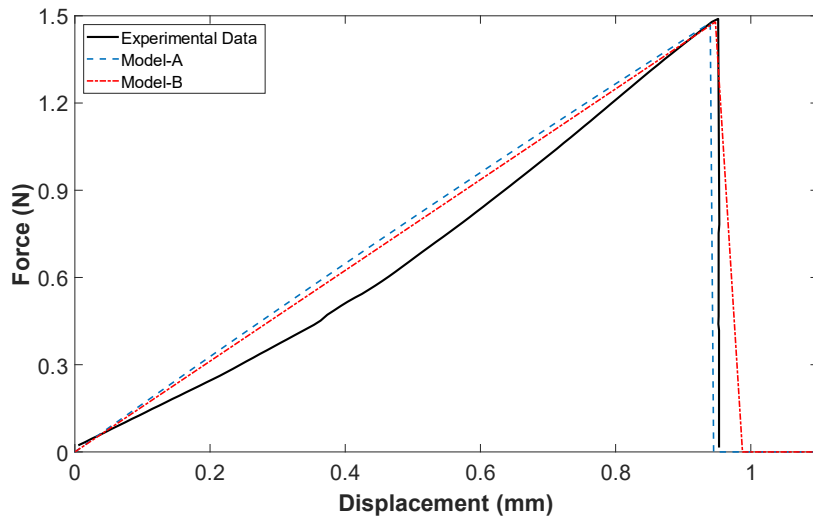


Figure 14 – Simulation results compared with single Vectran filament results (test data from [37]).

4.2.3 Multi-filament Kevlar Yarn

A multi-filament Kevlar yarn was then modeled using the same 1-D element approach in Abaqus and LS-Dyna to test whether the failure behavior of a multi-filament yarn could be predicted. Tensile test data was taken from Zhu et al. [38] where a 50 mm yarn of a single 380 denier Kevlar 49 with the diameter of 192.2 μm was tested. Figure 15 compares both Models A and B results with experimental data.

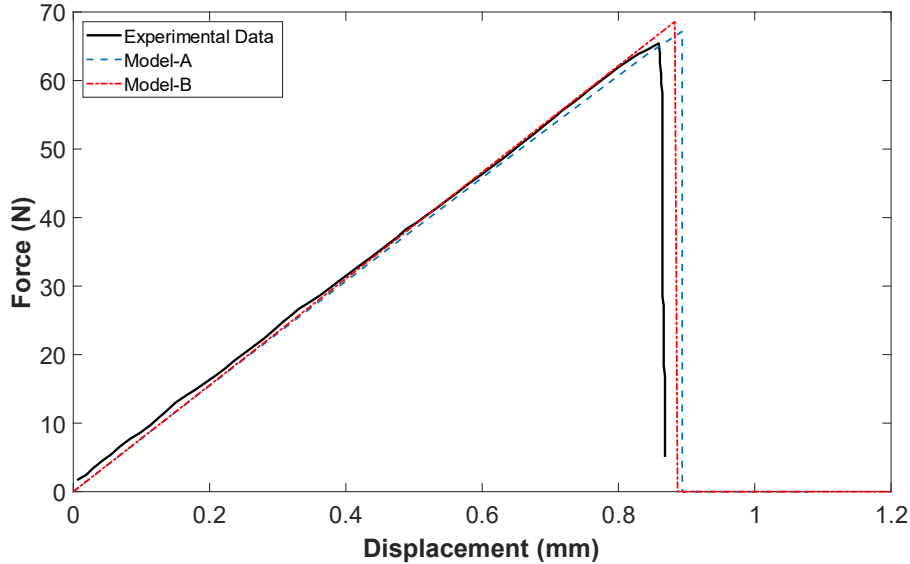


Figure 15 - Comparison of Models A and B with single Kevlar yarn results (test data from [38]).

A decrease in the hardening effect is observed when simulating a yarn, which consists of many filaments, as compared to the previous cases near the breaking point. The results compare well with the test data indicating that the FE models are capable of predicting the failure behavior of Kevlar yarns. The percent errors for failure load and displacement are found to be within 5% for both models. Provided in Table 2 is a summary of the material properties used in this study, and Table 3 includes the calculated errors for each test.

Table 2 – Material properties for different specimens used [35–38].

Test	Elastic Modulus (GPa)	Strength (GPa)	Density (kg/m ³)	Cross-sectional area (m ²)	Denier	Filament Count	Length (mm)
Carbon Filament	250	3.57	1774	4.20×10 ⁻¹¹	N/A	1	60
Kevlar Yarn	134	3.04	1440	2.90×10 ⁻⁸	380	256	50
Vectran Filament	88	3.43	1403	4.39×10 ⁻¹⁰	1500	1	25

Table 3 - Percent error calculated for the FE models.

Test	Maximum Force		Breaking Displacement		Fracture Energy Release Rate	
	Model A	Model B	A	B	A	B
Carbon Filament	1.56%	0.69%	2.38%	0.85%	7.57%	1.44%
Kevlar Yarn	2.69%	1.02%	4.02%	0.45%	3.82%	0.96%
Vectran Filament	0.93%	0.70%	1.23%	0.43%	10.15%	13.30%

5. T-cap Modeling

High-fidelity FE models of the T-cap structure were created in both codes using similar methodologies to predict the failure load and structure behavior during bending. Shell elements were used similar to the delamination methodology to model the individual laminates with thicknesses of 0.052 in (1.32 mm). Figure 16 presents the T-cap cross-section used to develop the geometries [9].

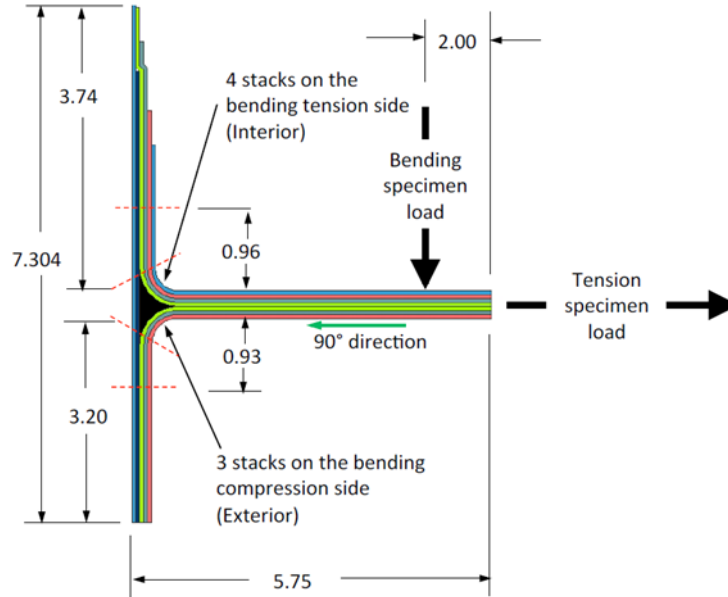


Figure 16 - T-cap cross-section used in the models (values are in inches) [9].

Each stack consists of material Class 72 Type 1 which is composed of AS4 fibers and VRM-34 epoxy resin. Table 4 includes the respective laminate properties used, with Table 5 incorporating unnotched laminate strengths [39]. Each stack of laminate consists of seven layers, defined as fiber directions [+45, -45, 0, 90, 0, -45, +45]. In the model, four stacks of the laminates were assumed on the tension side, and three on the compression side. The noodle section was modeled using fully integrated solid elements with IM6/3501-6 carbon epoxy properties.

Table 4 - DMS-2436D, Class 72 Type 1 laminate properties [39].

E_x (GPa)	E_y (GPa)	G_{xy} (GPa)	ν_{xy}
70.7	35.0	17.1	0.403

Table 5 – Unnotched laminate strengths [39].

X_T (MPa)	X_C (MPa)	Y_T (MPa)	Y_C (MPa)	S_C (MPa)
724.6	546.1	320.6	261.3	206.2

The respective composite damage models were applied in Abaqus and LS-Dyna to describe the composite behavior for the intra-laminar failure. Cohesive interaction (Tiebreak) was used to represent the VRM-34 epoxy for the inter-laminar failure. However, material properties of the VRM-34 epoxy were not publicly available. Modes I and II energy release rates, G , were implemented from the DCB tests conducted by Grenoble et al. [12]. Normal and shear peak traction values were implemented from the estimates made by Horton [7]. Hourglass controls were applied to keep any hourglassing energies below 10% [25].

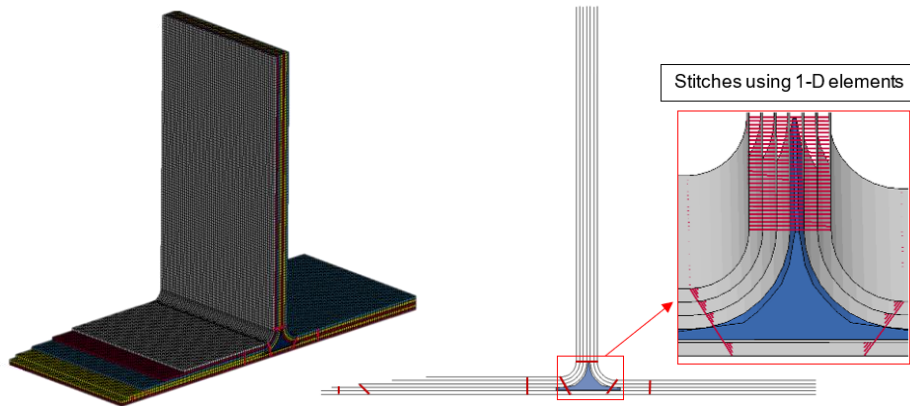


Figure 17 - FE model of the T-cap.

Figure 17 shows the FE model of the T-cap structure with theoretical thicknesses applied to the shell elements and highlights the stitching implemented using 1-D elements. The boundary conditions applied simplify the clamping of the T-cap structure at the base, similar to the bending test setup. A line load is applied at the same location where the pusher comes into contact with the T-cap structure. Stitches were implemented at the base of the T-cap models similar to the baseline specimen used in the bending test.

Medium and fine mesh models were investigated in the study. Medium mesh models had a mesh size of 0.1 in (2.54 mm) with 22,801 total number of elements. Fine mesh models had a size of 0.05 in (1.27 mm) with 89,356 total number of elements. The mesh sensitivity study underlined minimal effects on the results with further mesh refinements to 0.025 in and 0.01 in. To reduce the computational time needed to complete the simulation the width of the Abaqus T-cap model was reduced to 1.0 in.

6. Results

Results for Models A and B are shown in Fig. 18. The Butterworth filter was used in both analyses to remove the numerical noise [21]. The initial failure occurs as delamination damage near the noodle region at the base of the T-cap web where the plies began separating. The initial failure occurs sooner in the BNN1 test compared to the FE models, as shown in Fig. 18.

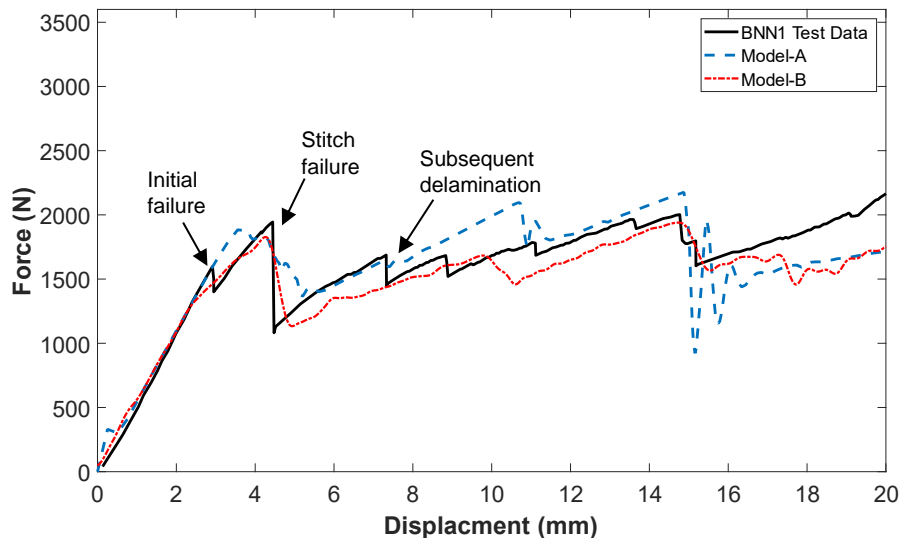


Figure 18 – Comparison of BNN1 test data [9] with T-cap simulation results.

Both FE models predict the onset of delamination after similar displacements of 4.8 mm for Model A and 4.3 mm for Model B. Model A has a small instability as the model initiates, before 1 mm of displacement, but then closely matches the initial test stiffness depicted at the beginning, refer to Fig. 19. Both models delaminate near the second failure point of the test data, capturing the initial

DAMAGE METHODOLOGY FOR HYBRID WING BODY AIRCRAFT STRUCTURES

peak force and load drop behavior. Model B captures the load drop particularly well due to the stitch failure that occurs shortly after initial delamination. Stitch failure does not occur at that point for Model A which is why the load drops more steadily than rapidly. Figure 19 shows the bending load sequence of the T-cap models.

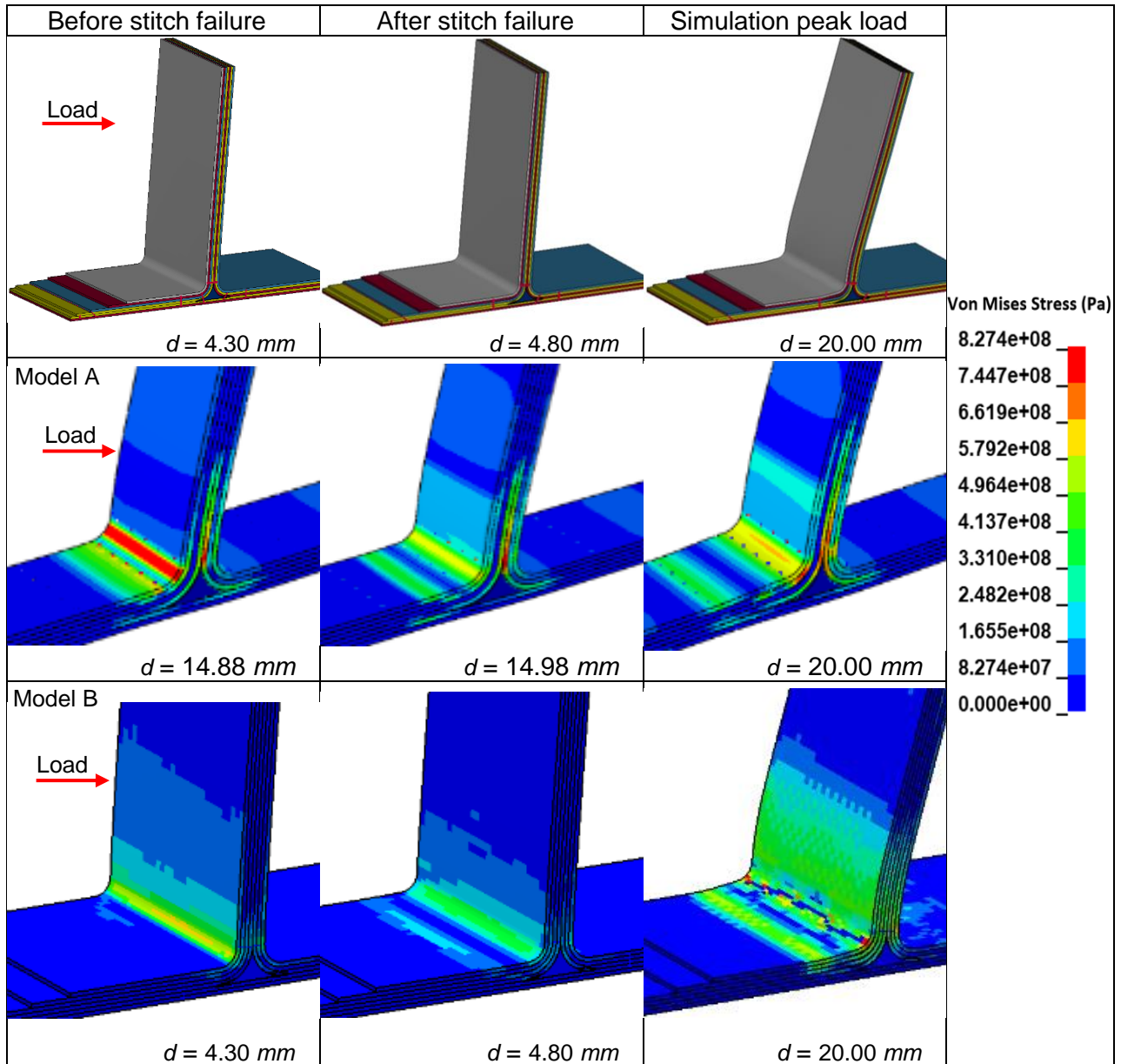


Figure 19 – Bending load sequence for the T-cap models.

Stitch failure occurs at different times for Models A and B as seen in Fig. 19. The first row of stitching, on the skin, on the tension side fails shortly after delamination initiates in Model B. Stitching at the same location fails at a later point in Model A. The stress range shown captures the peak stress in the laminates. The contours, however, do not show the maximum stress of the stitching due to the fixed bounds. Some elements are seen to fail in Model B near the bend on the first stack of the tension side. Comparatively, elements fail on the compression side near the bend for Model A. This could be due to the stitches failing much sooner in Model B, in comparison to Model A, where the stitch failure occurs after a 14.88 mm displacement. Stitches lasting longer in Model A could have resulted in prolonged damage arrest in tension and thereby delaying the failure on the tension side. Consequently, it could also be inferred that the effective tensile strength of Model B may be lower than that of Model A, which would lead to its failure in tension before failing in compression.

DAMAGE METHODOLOGY FOR HYBRID WING BODY AIRCRAFT STRUCTURES

Figure 20 shows the grayscale sequence of the approximate initial delamination near the noodle region. Qualitatively, Model B shows subsequent delamination which occurs between the two stacks on the tension side of the T-cap next to the noodle region. Contact force plots however confirmed that the initial delamination occurs near the noodle region in Model B. Figure 21 displays a grayscale sequence of the delamination propagation in both models. Stitching is scaled-up in Model A and marked with blue dash-lines in Model B for visual purposes. Stitching in Model B disappears (gets removed from the model) once failure occurs, whereas stitching in Model A remains visible after failure but carries zero stresses.

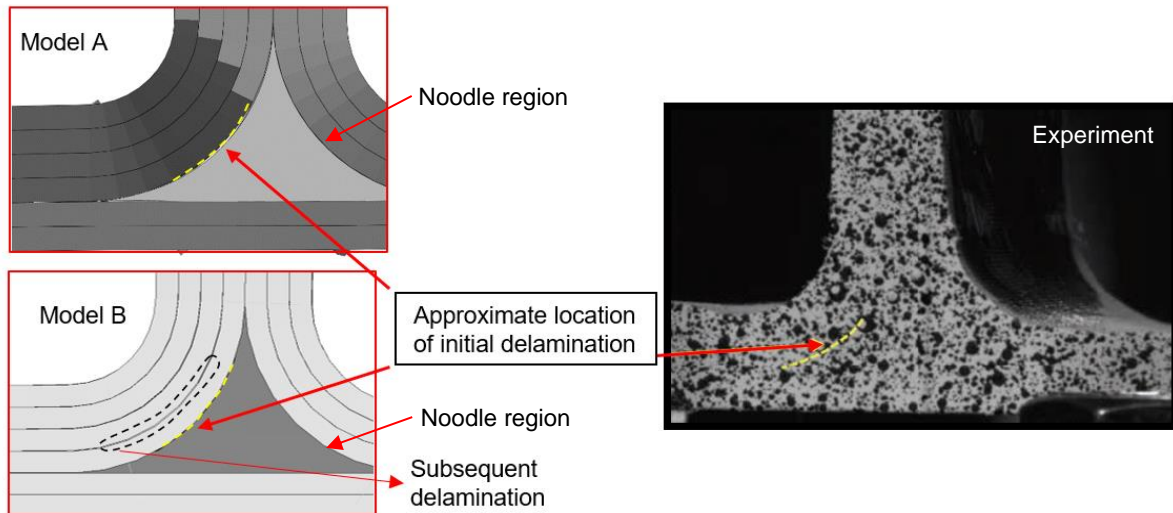


Figure 20 – Initial delamination in the FE models (left) compared with the BNN1 test [9] (right).

Before stitch failure	After stitch failure	Simulation peak load
Model A $d = 14.88 \text{ mm}$	$d = 14.98 \text{ mm}$	$d = 20.00 \text{ mm}$
Model B $d = 4.30 \text{ mm}$	$d = 4.80 \text{ mm}$	

Figure 21 – Grayscale sequence showing delamination propagation in the T-cap models.

7. Discussions and Conclusion

As the displacement was applied to the T-cap models, the load increased and dropped as failure due to delamination occurred. FE models determine the growth of delamination in the web region of the T-cap where they were arrested by stitching. Stitches in both models began taking larger portions of the load until they fail. The large load drops were associated with the failure of the stitching, whereas the smaller load drops represented the subsequent delamination after the onset. Both models did not capture the initial failure due to delamination, however successfully derived the subsequent and larger failure. Stitching in Model B failed shortly after the occurrence of the initial delamination, whereas the stitching failed at a later point in Model A. Due to the latter, the stitching in Model A was able to carry a larger load throughout the bending test than that of Model B, resulting in an overall higher load magnitude.

Subsequent delamination is captured by both models however not as evident since the load drops are not as prominent. This could be due to the simplifications made to the T-cap models where the

individual plies were not included as only the laminate stacks were modeled and thereby laminate level properties were utilized. This was a necessary simplification as modeling the individual plies would increase the computational cost significantly. Additionally, the cohesive interaction - Model A (Tiebreak - Model B) approach used for the interlaminar bonding between the laminates could have reduced the accuracy of the smaller load drops due to delamination as the approach approximates the interlaminar bonding. The tiebreak approach was chosen over the CZM due to its increased efficiency in terms of computation time. Finally, there is difficulty associated with measuring and modeling precise stitch interactions. The scarcity of the experimental data available for the 1600 denier Vectran thread makes it difficult to implement more accurate stitch behavior and properties compliant with the physical T-cap properties. The through-thickness effects of the stitching were not fully captured due to the simplification of modeling the stitches as 1-D elements where the load was only distributed to the top and bottom stack to which they were connected. Capturing the through-thickness effects of the stitching accurately would require more experimental data on stitch behavior, which was not readily available at the point when the study was conducted. Therefore, the simplification serves to provide a good overall representation of stitching implemented in the T-cap structure with the assumption that their through-thickness effects are small compared to their overall behavior with respect to the T-cap bending.

Despite the required simplifications, the models are able to capture the overall behavior of the T-cap bending test well and the important trends seen in the experiments. The initial failure in both models occurs near the second failure point of the test data, effectively predicting the initial peak force and delamination. The models were balanced between the accuracy and computational expense by utilizing laminate level details in the T-cap model and cohesive contact (Tiebreak) algorithms. Using laminate level details in the model allowed for sufficient precision in terms of the onset of damage and failure. The simplified stitching was able to arrest the delamination in both models effectively without significantly increasing the computational cost. Overall, the models were able to capture the intra- and inter-laminar failure of the T-cap structure when subjected to critical bending load.

Future work needs to include modeling the T-cap tension tests to predict the behavior of the joint under tension loading. Improvements could be made to the model by including ply level details where each individual unidirectional ply is modeled. This can increase the fidelity of the T-cap model and offer a better insight into the inter-laminar failure occurring due to delamination. Additional data on the stitches can contribute to the modeling methodology developed by accounting for the friction pull-out forces and through-thickness effects. This study provides a detailed damage methodology to predict the intra- and inter-laminar failure of the T-cap structures of PRSEUS under bending load for hybrid wing body aircraft structures.

8. Contact Author Email Address

Corresponding author:

Javid Bayandor; bayandor@buffalo.edu

9. Copyright Statement

The authors confirm that they, and/or their company or organization, hold copyright on all of the original material included in this paper. The authors also confirm that they have obtained permission, from the copyright holder of any third-party material included in this paper, to publish it as part of their paper. The authors confirm that they give permission, or have obtained permission from the copyright holder of this paper, for the publication and distribution of this paper as part of the ICAS proceedings or as individual off-prints from the proceedings.

10. Acknowledgments

The authors would like to highly acknowledge Ms. Dawn Jegley and Mr. Andrew Lovejoy from NASA Langley Research Center and Dr. Brandon Horton, previously at *CRASH* Lab, for their invaluable guidance on this topic.

References

- [1] Bayandor J., Johnson A., Thomson R. S., and Joosten M., Impact damage modelling of composite aerospace structures subject to bird-strike. *25th International Congress of the Aeronautical Sciences*, Hamburg, Germany, 2006.
- [2] Shah S., Bayandor J., Abdi F., and Najafi A., Micro mechanics based prognosis of progressive dynamic damage in advanced aerospace composite structures. *27th Congress of The International Council of The Aeronautical Sciences*, Anchorage, Alaska, USA, 2010.
- [3] Orifici A. C., Thomson R. S., Degenhardt R., and Bayandor J., The design of postbuckling composite aerospace structures accounting for damage initiation and growth. *26th International Congress of the Aeronautical Sciences*, Nice, France, 2008.
- [4] Velicki A. and Jegley D., PRSEUS Development for the hybrid wing body aircraft. *AIAA Centennial of Naval Aviation Forum "100 Years of Achievement and Progress"*, Virginia Beach, VA, 2011.
- [5] Leone F. A., Jegley D., and Linton K. A., Compressive loading and modeling of stitched composite stiffeners. *57th AIAA/ASCE/AHS/ASC Structures, Structural Dynamics, and Materials Conference*, San Diego, California, USA, 2016.
- [6] Felder J., Kim H., and Brown G., Turboelectric distributed propulsion engine cycle analysis for hybrid-wing-body aircraft. *47th AIAA Aerospace Sciences Meeting Including the New Horizons Forum and Aerospace Exposition*, Orlando, Florida, USA, 2009.
- [7] Horton B., Comprehensive multi-scale progressive failure analysis for damage arresting advanced aerospace hybrid structures. Ph.D, Virginia Tech, 2017.
- [8] Leone F. A. and Jegley D., Compressive testing of stitched frame and stringer alternate configurations. NASA/TM-2016-218974, NASA Langley Research Center, Hampton, VA, USA, 2016.
- [9] Lovejoy A. E. and Leone F. A., T-cap pull-off and bending behavior for stitched structure. NASA/TM-2016-218971, NASA Langley Research Center, Hampton, VA, USA, 2016.
- [10] Leone F.A., Pultruded rod/overwrap testing for various stitched stringer configurations. NASA/TM-2016-218975, NASA Langley Research Center, Hampton, VA, USA, 2016.
- [11] Velicki A., Yovanof N., Baraja J., Linton K., Li V., Hawley A., Thrash P., DeCoux S., and Pickell R., Damage arresting composites for shaped vehicles-phase II final report. NASA/CR-2011-216880, The Boeing Company, Phantom Works, Huntington Beach, CA, USA, 2011.
- [12] Johnston W. M. and Grenoble R., Material property characterization of AS4/VRM-34 textile laminates. NASA/TM-2013-218050, Hampton, VA, USA, 2013.
- [13] Dassault Systèmes, Abaqus analysis user's manual. Simulia Corp. Providence, RI, USA, 2020.
- [14] Kress G., Examination of Hashin's failure criteria for the second world-wide failure exercise. *Journal of Composite Materials*, Vol. 46, No. 19-20, pp 2539-2561, 2012.
- [15] Hashin Z., Failure criteria for unidirectional fiber composites. *Journal of Applied Mechanics*, Vol. 47, No. 2, pp 329-334, 1980.
- [16] Raza H., Garcia O.R., Carpenter K., Pärnänen T., Jokinen J., Kanerva, M. and Bayandor, J. Review of predictive methods for capturing onset of damage and initial delamination in carbon fibre reinforced polymer laminates subject to impact. *32nd Congress of the International Council of the Aeronautical Sciences*, Shanghai, China, 2021.
- [17] Wade B., Feraboli P., and Osborne M., Simulating laminated composites using LS-DYNA material model MAT54 part I: [0] and [90] ply single-element investigation. DOT/FAA/TC-14/19, Baltimore, MD, USA, 2012.
- [18] Chang F. K. and Chang K. Y., A progressive damage model for laminated composites containing stress concentrations. *Journal of Composite Materials*, Vol. 21, No. 9, pp 834-855, 1986.
- [19] Cherniaev A., Montesano J., and Butcher C., Modeling the axial crush response of CFRP tubes using MAT054, MAT058 and MAT262 in LS-DYNA®. *Proceedings of the 15th International LS-DYNA® Users Conference*, Detroit, MI, USA, 2018.
- [20] Livermore Software Technology Corporation (LSTC), LS-DYNA theory manual. Livermore, CA, USA, 2019.
- [21] Livermore Software Technology Corporation (LSTC), LS-DYNA keyword user's manual Manual Volume I. Livermore, CA, USA, 2020.
- [22] Dugdale D. S., Yielding of steel sheets containing slits. *Journal of the Mechanics and Physics of Solids*, Vol. 8, No. 2, pp 100-104, 1960.
- [23] Barenblatt G. I., The mathematical theory of equilibrium cracks in brittle fracture. *Advances in Applied Mechanics*, Vol.7, pp. 55-129, 1962.
- [24] Hui, C. Y., Bennison, S. J., and Londono, J. D. Crack blunting and the strength of soft elastic solids.

DAMAGE METHODOLOGY FOR HYBRID WING BODY AIRCRAFT STRUCTURES

Proceedings of the Royal Society of London. Series A: Mathematical, Physical and Engineering Sciences, Vol. 459, No. 2034, pp 1489-1516, 2003.

- [25] Siddens A. and Bayandor J., Multidisciplinary impact damage prognosis methodology for hybrid structural propulsion systems. *Computers & Structures*, Vol. 122, pp 178–191, 2013.
- [26] Turon A., Dávila C. G., Camanho P. P., and Costa J., An engineering solution for mesh size effects in the simulation of delamination using cohesive zone models. *Engineering Fracture Mechanics*, Vol. 74, No. 10, pp 1665-1682, 2007.
- [27] Bak, B. L., Sarrado, C., Turon, A., and Costa, J., Delamination under fatigue loads in composite laminates: a review on the observed phenomenology and computational methods. *Applied Mechanics Reviews*, Vol. 66, No. 6, p 24, 2014.
- [28] ASTM International, ASTM D5528-13, standard test method for mode I interlaminar fracture toughness of unidirectional fiber-reinforced polymer matrix composites. ASTM D5528-13, ASTM International, West Conshohocken, PA, USA, 2013.
- [29] Bayandor J., Thomson, R. S. and Callus P. J., Modelling the low velocity impact response of an aerospace composite replacement panel. *24th Congress of The International Council of The Aeronautical Sciences*, Yokohama, Japan, 2010.
- [30] Benzeggagh M. L. and Kenane M., Measurement of mixed-mode delamination fracture toughness of unidirectional glass/epoxy composites with mixed-mode bending apparatus. *Composites Science and Technology*, Vol. 56, No. 4, pp 439-449, 1996.
- [31] Lemmen P. and Meijer G.J., Failure prediction tool theory and user manual. TNO Report 2000-CMC-R0018, Ministry of Defense, Royal Netherlands Navy, Netherlands, 2004.
- [32] Mohamed G., Introduction to composites modelling in LS-Dyna. Arup, Solihull, West Midlands, UK, 2019.
- [33] Camanho P. P., Davila C. G., and de Moura M. F., Numerical simulation of mixed-mode progressive delamination in composite materials. *Journal of Composite Materials*, Vol. 37, No. 16, pp 1415-1438, 2003.
- [34] Celanese Acetate LLC, Vectran grasp the world of tomorrow engineering data. Charlotte, NC, USA.
- [35] Camanho P. P., Mixed-mode decohesion finite elements for the simulation of delamination in composite materials. NASA/TM-2002-211737, 2002.
- [36] Kumar R., Mikkelsen L. P., Lilholt H., and Madsen B., Understanding the mechanical response of glass and carbon fibres: stress-strain analysis and modulus determination. *IOP Conference Series: Materials Science and Engineering*, Vol. 942, No. 1, 2020.
- [37] Pegoretti A., Zanolli A., and Migliaresi C., Preparation and tensile mechanical properties of unidirectional liquid crystalline single-polymer composites. *Composites Science and Technology*, Vol. 66, No. 13, pp 1970-1979, 2006.
- [38] Zhu D., Mobasher B., Erni J., Bansal S., and Rajan S. D., Strain rate and gage length effects on tensile behavior of Kevlar 49 single yarn. *Composites Part A: Applied Science and Manufacturing*, Vol. 43, No. 11, pp 2021-2029, 2012.
- [39] Velicki A., *Damage arresting composites for shaped vehicles phase 1 final report*. NASA/CR-2009-215932, The Boeing Company, Huntington Beach, CA, USA, 2009.